NAVIER–STOKES SIMULATION OF DROPLET COLLISION DYNAMICS

M. Rieber and A. Frohn
(*iTLR* · Institut für Thermodynamik der Luft- und Raumfahrt,
Pfaffenwaldring 31, 70550 Stuttgart, Germany)

Abstract

A numerical method for the three-dimensional simulation of droplet collisions based on the volume-of-fluid (VOF-) formulation of the liquid-gas interface is presented. Important aspects of the numerical method with respect to accuracy, like second order interface reconstruction and conservative surface tension force approximation, and with respect to efficiency and robustness, like the multigrid Poisson solver used, are explained. For binary droplet collisions, the boundary between the regimes of coalescence and separation is determined numerically and compared with experiments in a wide parameter range. The energy balance during the collision process, which is not accessible to experiments, is determined numerically.

Introduction

Droplet collisions may have a strong impact on the evolution of the droplet size distribution in dense spray systems, such as sprays of fuel, water or liquid metal. While droplet collisions are a fundamental mechanical phenomenon, they are at the same time especially suited as benchmark test problems for free surface codes. Several experimental studies on droplet collisions supply detailed data, which depends only on a few well-defined physical parameters [1-3].

Three-dimensional droplet collisions have already been simulated successfully with the lattice–Boltzmann method [4]. This method is very efficient, but is limited to a relatively small range of Reynolds and Weber number. Numerical simulations with a front tracking method showed, that the topological changes inherent to droplet collisions are difficult to handle with the triangular mesh used to represent the interface [5]. The volume-of-fluid method used here does not suffer from such limitations, and is thus well-suited for the simulation of droplet collisions.

Numerical Method

The free surface flows considered here are governed by the incompressible Navier-Stokes equations

$$\nabla \cdot \mathbf{u} = 0 \,, \tag{1}$$

$$\frac{\partial \mathbf{u}}{\partial t} + (\mathbf{u} \cdot \nabla)\mathbf{u} = \frac{1}{\rho}(-\nabla p + \nabla \cdot \mathbf{S} + \mathbf{f}_{st}) \,. \tag{2}$$

In these equations, $\mathbf{u}$ is the velocity vector, p is the hydrodynamic pressure, and $\mathbf{S} = \mu[\nabla\mathbf{u} + (\nabla\mathbf{u})^T]$ is the viscous stress tensor. The density ρ and viscosity μ are constant inside each of the two fluids, but may vary discontinuously across the interface. The surface tension force $\mathbf{f}_{st}$ is added to the momentum equation as a body force, which is non-zero only in the interface region. The two-phase

related to the position of the interface, which is captured by means of the well–known volume–of–fluid method. This method introduces the volume fraction f of the liquid phase as additional dependent variable. The temporal and spatial evolution of the volume fraction is governed by the advection equation

$$\frac{\partial f}{\partial t} = -\nabla \cdot (\mathbf{u} f) \,. \tag{3}$$

The density and viscosity are obtained from the volume fraction f by the interpolations

$$\rho = \rho_g + (\rho_l - \rho_g) f \tag{4}$$

$$\mu = \mu_g + (\mu_l - \mu_g) f \,, \tag{5}$$

where the indices l, g refer to the liquid and gas phase, respectively. Starting from a solution $\mathbf{u}^n, p^n, f^n$ at time t^n or from initial conditions, which satisfy equation (1), the following first order time integration scheme is used to advance the solution from time t^n to time $t^{n+1} = t^n + \delta t^{n+1}$: (**I**) Solve the volume fraction advection equation (3) explicitly for f^{n+1}. (**II**) Solve the momentum equation (2) without the pressure term explicitly for an intermediate velocity field $\tilde{\mathbf{u}}$ using f^{n+1} for the calculation of the surface tension force. (**III**) Solve the Poisson equation

$$\nabla \cdot \left[\frac{1}{\rho^{n+1}} \nabla p^{n+1} \right] = \frac{\nabla \cdot \tilde{\mathbf{u}}}{\delta t^{n+1}} \tag{6}$$

for the new time level pressures p^{n+1}. (**IV**) Project the intermediate velocity $\tilde{\mathbf{u}}$ on the divergence-free velocity field $\mathbf{u}^{n+1}$ by adding the pressure source $-1/\rho^{n+1} \nabla p^{n+1}$.

Due to the explicit steps (**I**) and (**II**), the time step is limited at the beginning of each cycle according to

$$\delta t^{n+1} <= \min \left[\frac{h}{\max(\mathbf{u}^n)}, \sqrt{\frac{\rho_g + \rho_l}{4\pi\sigma}} h^{\frac{3}{2}}, \frac{h^2}{6 \max(\mu_l/\rho_l, \mu_g/\rho_g)} \right] \,, \tag{7}$$

which are time step constraints due to volume fraction and momentum advection, surface tension σ and momentum diffusion. For the droplet collisions considered here, the time step constraint due to surface tension is usually the most limiting one.

The spatial discretization is formally of second order accuracy, using second order upwind approximations for advection terms and central differences elsewhere. A non-equidistant staggered MAC-mesh is used (Fig. 1), which allows to satisfy the discrete equivalent to (1) exactly using a compact 7-point-Laplacian for the discretization of (6). For reasons of simplicity, the numerical method is explained here for grids with constant grid spacing h; corresponding illustrations are two-dimensional, sectional views. The remaining description of spatial discretizations concentrates on features specific to free surface flows. First the spatial discretization of the volume fraction advection equation (3) is examined in more detail. The volume fractions have values between zero and one only in a small transition region of a thickness comparable to the mesh size h (Fig. 2). This important property of the volume fractions is conserved by calculating the fluxes of the volume fractions across the cell faces based on an explicit interface reconstruction. While first-order reconstruction schemes like that of Hirt and Nichols [6] are still widely used, second order, piecewise linear interface reconstruction can improve results drastically. The reconstruction is performed for all partially filled cells in the domain by first calculating an approximation to the normal vector $\mathbf{n}$ on the interface. Then a plane cutting the cell is determined, which is perpendicular to $\mathbf{n}$ and which reproduces the exact volume fraction f of that cell (Fig. 2). Here the normal vector $\mathbf{n}$ on the interface is calculated from a finite difference approximation of

$$\mathbf{n} = \nabla f \tag{8}$$

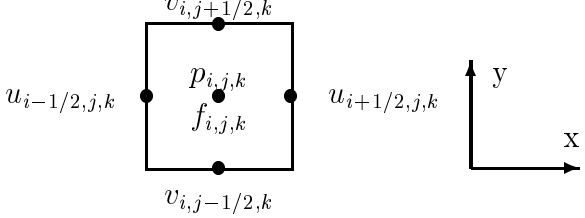

Fig. 1: The staggered MAC mesh. The pressure p and volume fraction f are located in the center of cell i, j, k, and the components of the velocity vector u, v and (not shown) w are located on corresponding cell faces.

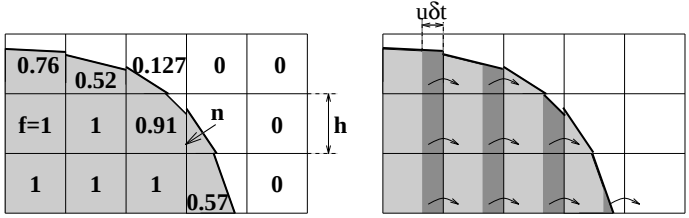

Fig. 2: Piecewise linear interface reconstruction based on the volume fractions f (left side) and volume fraction fluxes calculated for the x-sweep. In this example the velocity u has a constant positive value (right side).

using a 27-point-stencil. In this way a good approximation of the interface is obtained, as long as the maximum curvature is somewhat larger than $1/h$. The volume fractions are updated due to an operator split algorithm suggested by Puckett et al. [7], which has been extended to three dimensions. Before each one-dimensional sweep, the interface is reconstructed as explained above. Then a one-dimensional advection equation is solved, which for the x-sweep is

$$\frac{\partial f}{\partial t} = -\frac{\partial (fu)}{\partial x} + f\frac{\partial u}{\partial x} \,. \tag{9}$$

An illustration of the calculated volume fraction fluxes is given in figure 2. The "divergence" correction $f\partial u/\partial x$ is required, because f should behave as a Lagrangian invariant in each one-dimensional sweep. By alternately discretizing this correction implicitly and explicitly, the mass losses can be minimized[1].

The next point to examine is the surface tension force

$$\mathbf{f}_{st} = \sigma\kappa\hat{\mathbf{n}}\delta(\mathbf{x}-\mathbf{x}_s), \tag{10}$$

which is proportional to the surface tension σ and to the mean curvature κ. The surface tension force has the direction of the unit vector $\hat{\mathbf{n}} = \mathbf{n}/|\mathbf{n}|$, which points towards the center of curvature. The Dirac delta function δ localizes the force on the surface with coordinate $\mathbf{x}_s$. A possible non-conservative discretization of (10) is described by Brackbill et al. [9]. However, in the present paper the conservative approximation

$$\mathbf{f}_{st} = -\sigma\nabla\cdot\left[\frac{\tilde{\mathbf{n}}\,\tilde{\mathbf{n}}}{|\tilde{\mathbf{n}}|} - \mathbf{I}\,|\tilde{\mathbf{n}}|\right] \tag{11}$$

due to Lafaurie et al. [10] is preferred, because it behaves in a more physical way in under-resolved regions. The normal vector $\tilde{\mathbf{n}} = \nabla\tilde{f}$ is again calculated using a 27-point-stencil, where $\tilde{f}$ is a smoothed image of f as suggested in reference [9]. It has been found, that the total surface energy E_{st} can be easily approximated with the sum

$$E_{st} = \sigma \sum_{i,j,k\in\Omega} \sqrt{\tilde{\mathbf{n}}_{i,j,k}\cdot\tilde{\mathbf{n}}_{i,j,k}}\; h^3 \tag{12}$$

over the whole computational domain Ω. Furthermore, from this discrete definition of the surface energy, the discrete form of the surface tension force (11) can be derived. Thus any numerical error in the surface energy indicates a corresponding numerical error in the surface tension force. The validity of (12) can be shown for the continuous case $E_{st} = \sigma\int_\Omega |\nabla\tilde{f}|dV$, considering that $|\nabla\tilde{f}| = \delta(\mathbf{x}-\mathbf{x}_s)$.

[1] In two dimensions, this method leads to nearly exact conservation of mass [7].

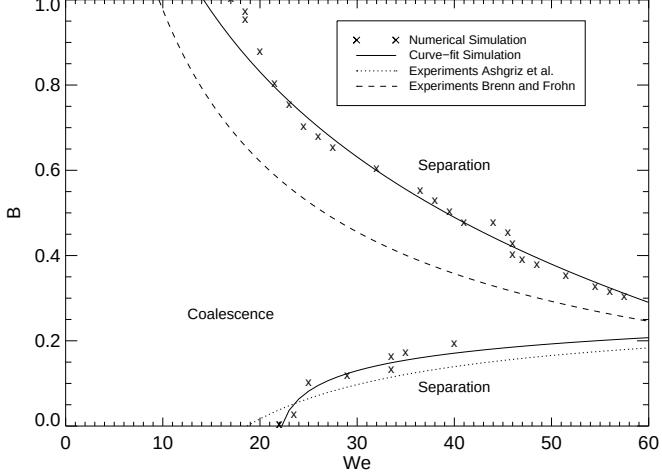

Fig. 3: Comparison between numerical and experimental results for the boundary between coalescence and separation in the B, We-space for the Reynolds number $Re = 5000$. The experimental results for the lower boundary are taken from reference [1].

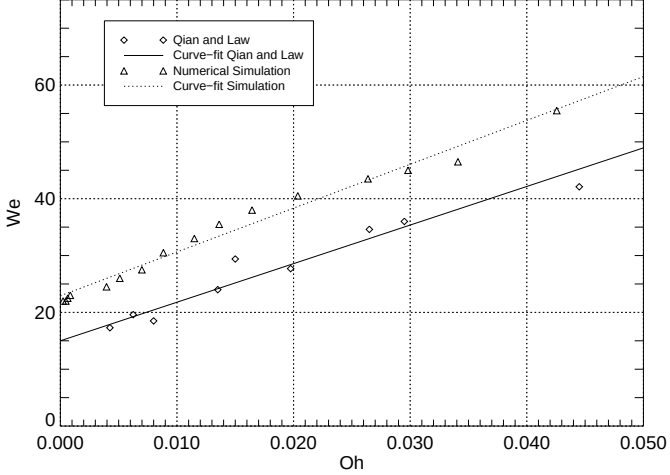

Fig. 4: Comparison between numerical and experimental results for the boundary between coalescence and separation in the We, Oh-space for central droplet collisions ($B = 0$). The experimental results are taken from reference [2].

The last problem to examine is the multigrid solver for the pressure Poisson equation. The matrix $\mathbf{A}$, which is constructed from a 7-point discretization of (6), has discontinuous coefficients according to the large density ratio between liquid and gas. This causes problems to standard multigrid Poisson solvers, and in fact often a degradation of the convergence rate in the case of high density ratios is reported [7, 10]. It has been found that the cell-centered multigrid algorithm MGCC suggested by Wesseling is rather insensitive to the density ratio [11]. With cell–centered multigrid[2], it is possible to construct a coarse grid matrix $\bar{\mathbf{A}}$ using the Galerkin approximation

$$\bar{\mathbf{A}} = \mathbf{R}\,\mathbf{A}\,\mathbf{P}\,, \tag{13}$$

which corresponds to a 7-point-Laplacian like the fine grid matrix $\mathbf{A}$. Therefore, the vectorizable red-black Gauss-Seidel smoother can be used for all multigrid levels. For the restriction operator $\mathbf{R}$ a linear interpolation is used, and for the prolongation operator $\mathbf{P}$ the adjoint of piecewise constant interpolation as in reference [11]. In the present code boundary conditions are not handled by modifying the operators near boundaries, but by using dummy cells. This facilitates parallelization of the code on distributed memory machines. However, with this treatment the restriction operator needs data from dummy cells. Therefore, appropriate mathematical boundary conditions for the matrix $\mathbf{A}$ and for the residual are needed. A homogeneous type of boundary conditions has been implemented, which leads to comparable residual reduction factors for both Dirichlet and Neumann conditions for the pressure. Depending on the problem solved, the residual norm is reduced by factors between 0.1 and 0.5 per multigrid v-cycle; usually between two and six multigrid v-cycles reduce the discrete velocity divergence sufficiently. For density ratios up to 10^5, no serious degradation of the convergence rate can be observed.

Results

The main dimensionless parameters for binary droplet collisions are the Weber number $We = \rho_l D\,U^2/\sigma$, the Reynolds number $Re = \rho_l D\,U/\mu_l$ and the geometrical collision parameter B, where D is the droplet diameter and U is the relative velocity of the droplets [1]. The value of the collision parameter is zero for central collisions and one for grazing collisions. Here only equally sized droplets are considered, so the ratio between the droplet sizes is not taken into account. The

[2]For cell-centered multigrid methods, every 8 cells of the fine grid are grouped together in one cell of the coarse grid.

Table 1: Parameters of presented simulations.

Case	B	We	Re	Resolution	Symmetries used
A	0	45	250	$64 \times 32 \times 32$	3
B	0.55	38	2500	$192 \times 128 \times 64$	1

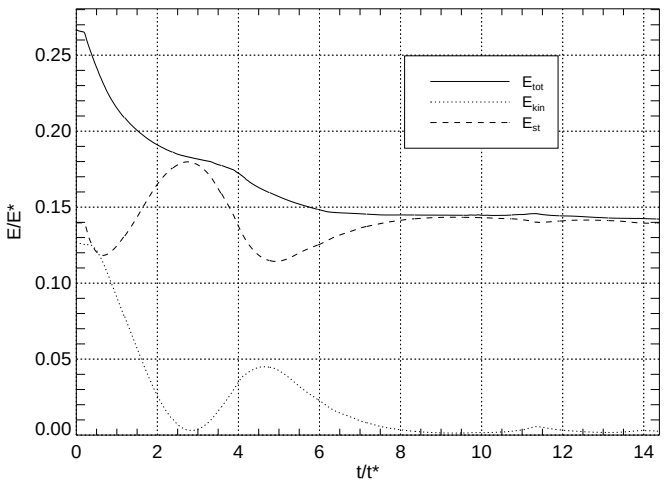

Fig. 5: Numerical results for kinetic energy E_{kin}, surface energy E_{st} and total energy E_{tot} of central droplet collision case (A) of table 1.

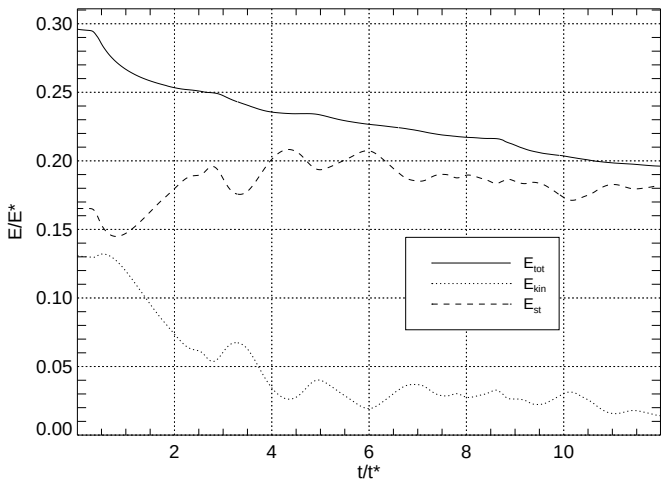

Fig. 6: Numerical results for kinetic energy E_{kin}, surface energy E_{st} and total energy E_{tot} of non-central droplet collision case (B) of table 1.

following results are based on the density and viscosity of a water-air system at normal conditions. Figure 3 shows computational results for the boundary between the regimes of coalescence and separation in dependency of We and B for the Reynolds number 5000. For this Reynolds number the semi-empirical results of Ashgriz et al. are available [1]. The lower boundary shows a very good agreement between numerical and experimental results. For the upper branch of the boundary own experiments have been used for the comparison [3]. The difference between numerical and experimental results is higher, but the general behavior is predicted very well. In fact, the deviation seems to be proportional to the collision parameter B. A possible explanation is, that with the volume-of-fluid method the droplets always melt together, as soon as their distance is smaller than h. For this reason, the momentum exchange, and thus energy losses, are higher than in reality.

The influence of the Reynolds number, or say, the Ohnesorge number $Oh = \sqrt{We}/Re$, is studied in figure 4. The numerical curve has nearly the same gradient but an offset towards higher Weber numbers. This offset can be identified with a constant additional viscosity of the numerical simulation in comparison to the experiment. A quantitative description of this offset however is an outstanding issue.

Two typical examples will illustrate the simulations needed to determine the boundaries between coalescence and separation. The parameters of the examples are given in Table 1. For both cases, symmetries were used to reduce computational costs. Thus, for case (A), only one eighth of the physical problem was simulated, and only one half for case (B). Case (A) is a central droplet collision with parameters near the regime of coalescence. For such a central collision, nearly all of the initial kinetic energy E_{kin} is dissipated, while the surface energy before and after the collision is that of two equal spheres [2]. The numerical simulation reproduces this fact, but at the same time gives further insight into the energy balance during the droplet collision, as shown in figure 5. In this and all following figures, time and energy are measured in units of $t^* = D/U$ and $E^* = \rho_l D^3 U^2$, respectively. Because the system is closed in the present case, the total energy $E_{tot} = E_{st} + E_{kin}$ has to decrease monotonically. Any other numerical result for the total energy would indicate inaccurate results. Thus the energy balance can be used as a monitoring tool for the simulation. For example, convergence of the numerical simulation with respect to the grid resolution may be checked easily

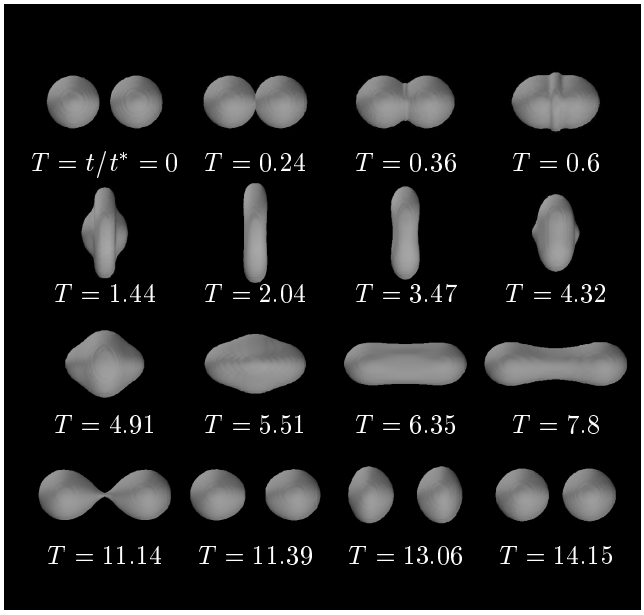

Fig. 7: Temporal evolution of droplet shapes for the central droplet collision case (A) of table 1.

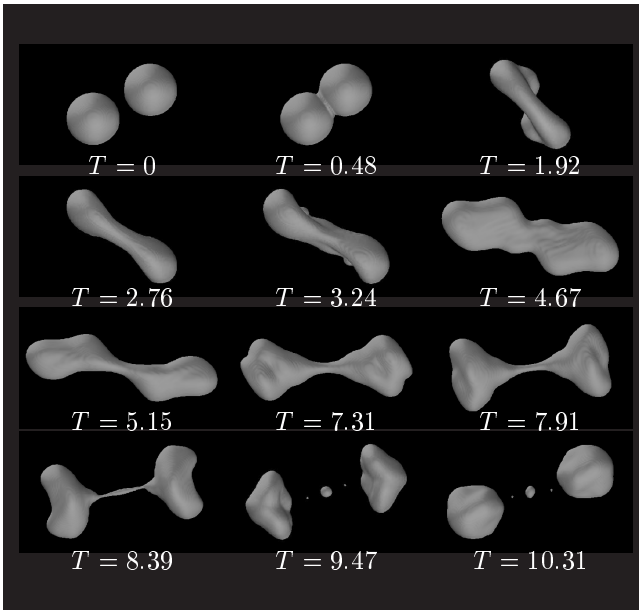

Fig. 8: Temporal evolution of droplet shapes for the non-central droplet collision case (B) of table 1.

with the help of the energy balance. The temporal evolution of the droplet shapes shown in figure 7 compares well with experiments of Qian and Law [2].

Case (B) is a non-central droplet collision, again with parameters near the regime of coalescence. In this case, the total energy again is decreasing monotonically, however, with a smaller rate compared to case (A). This is not only due to the higher Reynolds number, but also due to less shearing of the liquid. The higher Reynolds number allows a longer existence of higher deformation modes, which is clearly visible from both the energy balance and the droplet shapes (Figures 6 and 8). The formation of the satellite droplet was not predicted for lower resolutions, thus indicating, that the resolution of $192 \times 128 \times 64$ cells was at least needed.

In future work collisions between droplets of different size will be investigated in order to achieve results of more practical relevance. Such results would be important in many multi-phase codes which need exact models for droplet collisions.

References

[1] Ashgriz, N. and Poo, J. Y., *J. Fluid Mech.*, **221** (1990), 183–204.

[2] Qian, J. and Law, C. K., *J. Fluid Mech.*, **331** (1997), 59–80.

[3] Brenn, G. and Frohn, A., *Experiments in Fluids*, **7** (1989), 441-446.

[4] Schelkle, M., Rieber, M. and Frohn, A., *2nd Int. Symp. on Numerical Methods for Multiphase Flows, ASME Fluids Engineering Division*, (1996).

[5] Nobari, M. R. H. and Tryggvason, G., *AIAA Journal*, **34**(49) (1996), 750–755.

[6] Hirt, C. W. and Nichols, B. D., *J. Comp. Phys.*, **39**(1) (1980), 201-225.

[7] Puckett, E. G., Almgren, A. S., Bell, J. B., Marcus, D. L. and Rider, W. J., *J. Comp. Phys.* **130** (1997), 269–282.

[9] Brackbill, J. U., Kothe, D. B. and Zemach C., *J. Comp. Phys.*, **100** (1992), 335–354.

[10] Lafaurie, B., Nardone, C., Scardovelli, R. and Zaleski, S., *J. Comp. Phys.*, **113** (1994), 134–147.

[11] Wesseling, P., *J. Comp. Phys.*, **79** (1988), 85–91.